Theoretical analysis of R-line shifts of ruby subjected to different deformation conditions

Surinder M. Sharma* and Y. M. Gupta
Shock Dynamics Laboratory, Department of Physics, Washington State University, Pullman, Washington 99164-2814
(Received 13 August 1990)

A theoretical approach to analyzing ruby R-line wavelength shifts under different types of deformation (uniaxial-strain compression and tension under shock loading, hydrostatic compression, and uniaxial-stress compression) and for different crystallographic orientations is presented. A symmetry-adapted representation of the various loading conditions in conjunction with crystal-field theory, but no point-ion model, is used to relate the shift of the R lines to deformation. The parameters needed in the model are obtained from shock-wave-compression data along the c and a axes. Without further iteration, these parameters are used in a consistent manner to analyze all remaining data: shock-wave-tension results, hydrostatic results, and uniaxial-stress results for different crystal orientations. Very good agreement is obtained between theoretical predictions and measurements. Changes in local site symmetry have been related to macroscopic deformation. For nonhydrostatic loading, effects of crystal orientation are important in analyzing R-line wavelength shifts. Suggestions for using ruby calibration at high pressures in diamond-anvil-cell measurements are presented. Implications of the present work for understanding shock-wave deformation in crystalline solids are indicated.

I. INTRODUCTION

The optical spectrum of ruby (Al_2O_3:Cr^{3+}), at ambient conditions, has been investigated extensively in spectroscopic studies,[1-4] and there exists a good understanding of the spectral details in terms of crystal-field theory.[2,3,5-7] The ruby R lines (originating from the ^2E level), because of their sharpness and sensitivity to pressure,[8] are now used routinely for pressure calibration into the megabar range in static pressure studies utilizing the diamond anvil cell (DAC).[9-13] At higher pressures the state of stress in the DAC is not hydrostatic, and a good understanding of the effects of nonhydrostatic stress on the R-line shift is of considerable interest. The effect of uniaxial stress along the c and a axes, at very low stresses,[14,15] on the ruby R lines had been examined prior to the use of ruby for pressure calibration in an attempt to gain insight into the nature of the local environment around the Cr^{3+} ion in Al_2O_3. Recently, experimental methods have been developed in our laboratory to examine the R-line shifts under shock loading.[16] Shock-wave experiments, though inherently difficult, can permit an examination of the R lines in samples subjected to well-defined uniaxial strain (but strongly nonhydrostatic stress) states along different crystallographic orientations. Shock-wave experiments[17-19] have been carried out in which both c- and a-axis ruby crystals have been subjected to 125 kbar longitudinal stress in compression and 110 kbar in tension. Given the hydrostatic, uniaxial-stress, and uniaxial-strain data, it is desirable to understand the R-line response to different loading conditions.

The present work had two main objectives: (a) to develop a theoretical framework to analyze and understand the R-line data under different loading conditions in a consistent manner, and (b) to examine the possibility of using the optical spectra as a microscopic probe of shock-induced changes in crystalline solids. Shock-wave experiments provide information about continuum and thermodynamic properties, but little information, if any, exists regarding shock-induced processes at the atomic and/or molecular level. The use of optical spectroscopy under shock loading to obtain this information is a promising but new undertaking. The present work represents a start toward describing shock-induced deformation in solids in terms of local-site-symmetry changes.

There have been two first-principles calculations to understand the behavior of R lines. In both calculations a cluster of Cr^{3+} ions and surrounding atoms was embedded in the host lattice. Ohnishi and Sugano[20] carried out their calculation using the discrete variational x_α method. They embedded an octahedral $(CrO_6)^{9-}$ cluster in a flat potential well to represent ruby. The calculated redshift of the R lines was in reasonable agreement with experiments. The subsequent calculation by Shangda *et al.*[21] is for ambient conditions, but models the ruby more realistically. The Cr^{3+}, or various clusters involving Cr^{3+}, is embedded in the proper Al_2O_3 crystal potential. These results indicate that the good agreement in Ref. 20 may be accidental. This latter calculation,[21] despite disagreement with experimental results, emphasizes the need to relax the atoms around the Cr^{3+} to obtain even qualitatively meaningful results.

Crystal-field theory, though phenomenological, has been reasonably successful in understanding the nature of deformation-induced variations. R_1-R_2 splitting can be written in terms of stress-induced changes in the trigonal field for stress along the c axis.[22] Point-ion-model estimates of stress splittings of impurities in rocksalt lattices have been reasonably successful.[22,23] For ruby these splittings had not been calculated because of the

 ©1991 The American Physical Society

difficulties in getting the correct sign for the trigonal field at ambient conditions.[3,15] However, our estimates of the splitting change for hydrostatic pressure give a reasonable agreement with observed results.[24]

The redshift of R lines under hydrostatic pressure has been modeled using scaling theories.[25–28] The scaling theories, in essence, use a renormalized point-ion crystal-field model; the parameters vary with interatomic distances as for a point-ion model, but with the coefficients suitably altered to be determined from fit to experimental data. Scaling of parameters has been carried out for isotropic deformation. It is difficult to generalize the scaling theories to anisotropic deformation because a general anisotropic deformation is a tensor of second rank.

Our approach to understanding the shift of the R lines to different deformation conditions is based on the general framework of crystal-field theory; the point-ion model, however, is not used. We have chosen a symmetry-adapted description for different strain conditions to analyze the optical spectra. Parameters characterizing the effects of various irreducible strain tensors on the R lines are obtained using data from shock-wave-compression experiments along the c and a axes.[17,19] All subsequent calculations used for predicting the uniaxial-strain tension results, hydrostatic stress, and uniaxial-stress results are then based on these parameters without any iteration. Although some of the developments presented here may be applicable to other parts of the ruby spectrum, we are confining the present work to the R lines. Hence discussion[29–33] regarding the absorption bands and other lines will not be presented here.

Section II presents a compilation of shock-wave results needed for subsequent analysis. Section III presents relevant background regarding crystal structure and ambient spectrum. Section IV describes the theoretical developments to analyze the effects of external deformation on the R lines. Evaluation of the parameters for the theoretical model and analyses of experimental data are presented in Sec. V. Discussions and conclusions regarding the present work are presented in Sec. VI.

II. SUMMARY OF UNIAXIAL-STRAIN RESULTS

A summary of experimental data[17–19] from shock-wave uniaxial-strain experiments along the c and a axes is presented here for use in the subsequent sections. The compression data range up to a longitudinal stress of 125 kbar (approximately 2.5% density change), and the tension data range up to a longitudinal stress of 108 kbar (approximately 2.2% density change). Details regarding the experimental methods and results are given elsewhere.[17–19]

In the following the spectral quantities are in units of cm^{-1} and the density strain is defined as $\mu \equiv \rho/\rho_0 - 1$. The error bars refer to 95% confidence limits to the fits.

A. c axis

The shifts for the R_1 and R_2 lines for both compression and tension can be fitted as

$$\Delta\nu_1 = 0.519(\pm 0.34) - 1493.9(\pm 17.5)\mu - 16\,492.5(\pm 1167)\mu^2 , \quad (1)$$

$$\Delta\nu_2 = -0.312(\pm 0.24) - 1715.6(\pm 11.9)\mu - 16\,186.3(\pm 805)\mu^2 . \quad (2)$$

The average of the R_1 and R_2 shifts, and R_1-R_2 splitting from Eqs. (1) and (2) is given by

$$\Delta\nu = 0.21(\pm 0.41) - 1604.7(\pm 21)\mu - 16\,339.4(\pm 1418)\mu^2 , \quad (3)$$

$$\Delta(R_1 - R_2) = 29.6 - 221.7(\pm 21)\mu + 306.3\mu^2 . \quad (4)$$

The constant term in Eqs. (1)–(3) should be zero; the small value reflects merely the ± 1 cm^{-1} precision of the experimental data. Similar remarks apply to the a-axis data below.

B. a axis

The average of the R_1- and R_2-line shifts for both compression and tension could be fitted to a single curve given by

$$\Delta\nu = 0.68(\pm 0.31) - 2163.8(\pm 12.2)\mu - 11\,453(\pm 993)\mu^2 . \quad (5)$$

Because of the strongly nonlinear response of splitting for shock compression along the a axis, a single equation cannot be fitted to the splitting data. Hence the compression and tension data along the a axis are presented as follows:

compression:

$$\Delta\nu_1 = -2420.2(\pm 21)\mu - 16\,669(\pm 1035)\mu^2 , \quad (6)$$

$$\Delta\nu_2 = -2104.1(\pm 25)\mu ; \quad (7)$$

tension:

$$\Delta\nu_1 = -2042.8(\pm 80)\mu - 25\,739.6(\pm 4228)\mu^2 , \quad (8)$$

$$\Delta\nu_2 = -1920.6(\pm 112)\mu - 18\,202(\pm 5886)\mu^2 . \quad (9)$$

Comparison of Eqs. (6) and (7) to Eqs. (8) and (9) shows that for a given value of density compression μ, the change in line splitting can be written as

$$\Delta(R_1 - R_2)|_{\text{comp}} > \Delta(R_1 - R_2)|_{\text{tens}} . \quad (10)$$

Over the stress range indicated here, the response of the ruby is completely elastic. The above data have been corrected[17] for the very small temperature change (≈ 10 K) due to shock compression in room-temperature experiments.

C. Curvature and asymmetry in shock results

For completeness two aspects of the shock-wave results that are analyzed in Sec. V are indicated here. Further details may be seen in Ref. 19. Over the hydrostatic pressure range (to 150 kbar) considered in the paper by Munro *et al.*[10] and others,[9,13] the R lines shift linearly with pressure (or mean stress). In the shock experiments, the

R lines shift nonlinearly with mean stress and the observed curvature reflects the changes in local site symmetry due to nonhydrostatic deformation. This observed curvature is analyzed in the present paper.

Because hydrostatic data exist only for compression, we have extrapolated these into tension to permit comparisons with shock data. Comparison of the hydrostatic results in compression and tension with the mean of R_1- and R_2-line shifts under shock loading show an interesting variation with crystal orientation. For shock compression along the c axis, the mean shift deviates away from the extrapolated hydrostatic results in tension. For shock compression along the a axis, the mean shift deviates away from the hydrostatic results in compression. This asymmetry again reflects the changes in local site symmetry and is analyzed here.

III. BACKGROUND

A. Crystal structure

Ruby has a corundum structure[34] [$R\bar{3}C$ (No. 167)] with aluminum along the threefold axis. Cr^{3+} replaces Al^{3+} substitutionally, and at 0.1% atomic concentration there is approximately one chromium atom per 60-unit cells. It is difficult to determine the exact atomic coordinates of Cr^{3+} in dilute ruby. X-ray-diffraction studies[35,36] of samples with higher chromium concentrations (4% and 5.2%) indicate that the chromium is located on the trigonal axis, but may be shifted slightly toward the nearest aluminum neighbor. Because all of the shock experiments have been carried out on dilute ruby (0.3–0.4 % concentration), it is difficult to ascertain the validity of this finding for the present work.

The structure of ruby[37,38] and sapphire[39] has been examined as a function of hydrostatic pressure up to approximately 100 kbar. The ruby results were reanalyzed by Kottke and Williams[40] to show that the c axis is more compressible by approximately 12%, in agreement with the macroscopic compliance constants for sapphire.[41] For dilute ruby samples of interest to the present work, the macroscopic elastic constants are taken to be the same as those for sapphire (α-Al_2O_3).

The first-neighbor O^{2-} ions form almost an octahedron with respect to the Cr^{3+} ion; a very small change in the positions of the first neighbors would make the arrangement exactly octahedral. In this hypothetical unit, a system of Cartesian axes can be centered on Cr^{3+} such that the six O^{2-} ions are along the xyz axes, at a distance $\pm R$ from the Cr^{3+} ion. Looking down the threefold axis [111] of this octahedral arrangement, the hypothetical unit looks as shown in Fig. 1. The two sets of triangles define planes (containing the O^{2-} ions) above and below the Cr^{3+} ion. The xyz axes shown in Fig. 1 are projections of the orthogonal axes in the plane of the figure. For subsequent discussion it is convenient to define a coordinate system XYZ, in which the Z axis coincides with the crystallographic c axis[42,43] (or the threefold axis of the octahedral xyz system) and the X and Y axes are obtained by a 60° rotation of the crystallographic a and m axes about the crystallographic c axis.

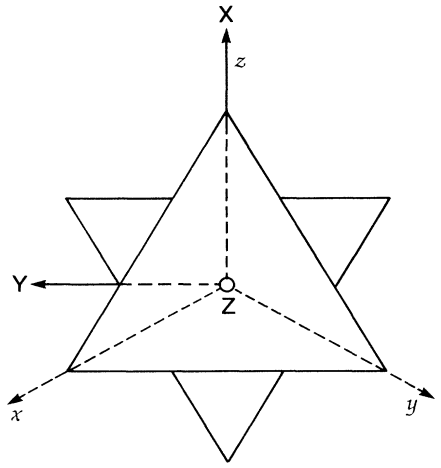

FIG. 1. Different crystallographic systems used in the theoretical analysis. The two sets of triangles define planes containing oxygen ions above and below the Cr^{3+} ion. The XYZ system is referred to as the trigonal system. This figure is similar to Fig. 6.2 in Ref. 45.

In the actual structure, the two sets of triangles shown in Fig. 1 are rotated (around Z) away from each other by a 3°54′ angle and all the oxygens are not equidistant. The displacement of Cr^{3+} ions with respect to the host Al^{3+} sites, as observed in high-concentration ruby, makes the arrangement more octahedral. However, distant neighbors do not conform to an octahedral arrangement, and only threefold symmetry exists. For a description of the properties which arise from the localized nature of the d electrons, the nearest neighbors have the dominant effect; this conclusion is confirmed by analysis of the ambient spectrum.[2,5–7]

B. Ambient spectrum

For discussing the localized electronic states of Cr^{3+}, the Hamiltonian can be written as[44]

$$H_{\text{total}} = H_{\text{octahedral}} + H_{\text{trig}} + H_{\text{SO}} \ . \tag{11}$$

H_{oct} includes all the interactions which conform to octahedral or higher symmetry, H_{trig} is invariant with respect to C_3 symmetry, and H_{SO} represents the spin-orbit interaction. Because of the complexity of the crystal structure, H_{trig} in Eq. (11) is expected to be a complicated operator. It includes the interaction of Cr^{3+} with more distant neighbors as well as the effect of distortion of the local octahedron to generate the actual atomic arrangement. Hence an analytic representation of H_{trig} may be very difficult, but Eq. (11) can be used to present all the necessary interactions in a phenomenological manner.

The analysis[2,5–7] of the ruby spectrum at ambient conditions shows that the effects of H_{trig} and H_{SO} can be treated as perturbations with respect to that of $H_{\text{octahedral}}$.

For use in subsequent analysis, we briefly discuss, using the developments in Ref. 45, the effects these perturbative terms have on the energy of $t_2^3:{}^2E$ states which give rise to the R lines.

In the absence of spin-orbit interaction and trigonal field, the energy of the ^2E state depends only on electron-electron repulsion[45] characterized by the Racah parameters B and C. The presence of the above-mentioned perturbative interactions couple ^2E and $^2T_2$ states within the t_2^3 configuration.[2] The effect of this coupling may be calculated using second-order perturbation theory by evaluating the following matrix elements:[45]

$$\sum_{M_s'',M''} \frac{\langle t_2^3\,{}^2EM_s'M'|H_{\text{pert}}|t_2^3\,{}^2T_2M_s''M''\rangle\langle t_2^3\,{}^2T_2M_s''M''|H_{\text{pert}}|t_2^3\,{}^2EM_sM\rangle}{\epsilon(^2E)-\epsilon(^2T_2)} , \tag{12}$$

where the notation $t_2^3\,{}^2E$ represents the ^2E state arising from three electrons in t_{2g}-type states, M_s represents the magnetic quantum number, and M denotes the basis of ^2E as u_+ and u_- and of $^2T_2$ as x_+, x_-, and x_0.

Matrix elements of Eq. (12) are calculated, as shown in Chap. 8 of Ref. 45, by using the Wigner-Eckart theorem:

$$\langle \alpha\Gamma\gamma|X_{\gamma''}(\Gamma'')|\alpha'\Gamma'\gamma'\rangle=(\Gamma)^{-1/2}\langle \Gamma\gamma|\Gamma'\gamma'\Gamma''\gamma''\rangle\langle \alpha\Gamma\|X(\Gamma'')\|\alpha'\Gamma'\rangle , \tag{13}$$

where the second factor on the right represents Clebsch-Gordan coefficients, tabulated in Ref. 45, and the double-barred elements are "reduced matrix elements" tabulated in Ref. 5. For matrix elements of interest to the present work, the following quantities have been evaluated in Ref. 45: $\langle t_2^3\,{}^2E\|H_{\text{trig}}\|t_2^3\,{}^2T_2\rangle=-6K$, where $3K\equiv\epsilon(E)-\epsilon(A_1)$, and $\langle t_2^3\,{}^2E\|H_{\text{SO}}\|t_2^3\,{}^2T_2\rangle=-\sqrt{6}i\zeta$, where $\zeta=-2\langle t_{2g}1/2, x_+|H_{\text{SO}}|t_{2g}1/2, x_+\rangle$. Using these results, the shift of the ^2E state due to the trigonal field is given by

$$\Delta(\epsilon(^2E))=\frac{-6K^2}{\epsilon(^2T_2)-\epsilon(^2E)} . \tag{14}$$

The coexistence of the trigonal field and spin-orbit interaction splits ^2E states into the Kramers' doublets $^2E(\bar{A}_1+\bar{A}_2)$:$\pm 1/2u_\pm$ and $^2E(\bar{E})$:$\pm 1/2u_\mp$ associated with the R_2 and R_1 lines, respectively. The R_1-R_2 splitting is given by

$$\epsilon(^2E(\bar{A}_1+\bar{A}_2{:}R_2))-\epsilon(^2E(\bar{E}{:}R_1))=\frac{4K\zeta}{\epsilon(^2E)-\epsilon(^2T_2)} . \tag{15}$$

In recent papers, the trigonal field is represented by v and v' using the definition by Pryce and Runcimen:[46] $v=-3\langle t_{2g}x_+|v_{\text{trig}}|t_{2g}x_+\rangle$ (and for the configuration interaction $v'=\langle t_{2g}x_+|v_{\text{trig}}|e_gu_+\rangle$). It can be shown that $v=-3$ K, and the above results can be easily written in terms of v. For subsequent numerical calculations in Sec. V, the following comments are helpful: K in Eq. (15) is a negative quantity because the denominator as written is negative; an increase in the trigonal field causes K to be more negative (ΔK is negative and Δv is positive) and results in increased line splitting. The redshift due to the trigonal field in Eq. (14) depends only on the magnitude of K or v.

Inclusion of a configuration interaction changes Eqs. (14) and (15) somewhat. For the strong-field approximation, this calculation has been carried out by Sugano and Peter,[5] and for the weak-field approximation the calculation has been carried out by Macfarlane.[6,44] Because of a lack of information about how the parameters characterizing configuration interaction, viz. v' and ζ', change, these corrections are not considered in the present work. This issue is commented upon in Sec. VI.

IV. THEORETICAL FORMULATION

To evaluate the effect of external strains, it is necessary to relate these to changes in the interaction Hamiltonian. The idealized, first-neighbor interaction, described by octahedral symmetry, provides a good unperturbed description of the ^2E state. Hence we shall use this as the basic symmetry, which is then perturbed by external strain or stress. The effect of ambient distortions is taken as additive in the spirit of Eq. (11). Because the change in the interaction Hamiltonian depends directly on strain, we formulate the problem in terms of strain. Throughout this paper strains will be assumed to be positive in compression and negative in tension.

A. Symmetry-adapted strains

The transformation properties of a strain tensor, due to its second rank, are the same as that of a dyadic—the product of Cartesian coordinates. Hence there exists a one-to-one correspondence between the components of the strain tensor and the symmetry-adapted d-electron wave functions for the octahedral group; the latter have been presented in Chap. 2 of Ref. 45. The symmetry-adapted d orbitals can be classified according to irreducible representations (T_2,E, A) of the octahedral group. The one-to-one correspondence between the basis functions for the d electrons and the strain tensor components permits a decomposition of the strain tensor into similar irreducible components. Using this approach, the six independent strain components are grouped into three sets as shown in Table I. In the notation used, the symbols in parentheses represent the irreducible representation (IR) and the subscripts represent basis functions in that IR. Similar symmetry-adapted strains in conjunction with the point-ion model were used by Schawlow, Piksis, and Sugano[23] to calculate the uniaxial-stress response of the

TABLE I. Strains in the octahedral basis.

Strain component	Transformation	Characteristic feature
(1) $e(A_1)$	$x^2+y^2+z^2$	preserves octahedral symmetry
(2) $e_u(E)$	$2z^2-x^2-y^2$	tetragonal distortion with respect to the z axis
(3) $e_v(E)$	x^2-y^2	rhombic distortion preserving reflection symmetry with respect to the xz and yz planes
(4) $e_\xi(T_2)$	yz	rhombic distortion preserving mirror with respect to a plane $\perp yz$ plane and passing through $y=z$ or $y=-z$
(5) $e_\eta(T_2)$	zx	analog of 4
(6) $e_\zeta(T_2)$	xy	analog of 4

spectrum of Cr^{3+} in magnesium oxide (rocksalt structure). The geometric nature of the various distortions is shown in Fig. 2. While the equivalence of the three T_2 strains is transparent, the equivalence of E-type strains would require appropriate linear combinations, similar to those for the wave functions.[47]

For analyzing the deformation in ruby, it is more convenient to carry out the theoretical analysis with respect to the XYZ system (referred to as the trigonal axes) indicated in Fig. 1 and discussed on p. 131 of Ref. 45. In this system the Z axis is parallel to the crystallographic c axis and the X axis makes an angle of 60° with respect to the crystallographic a axis. The symmetry-adapted strains in Table I can be transformed to refer to the new axes. The irreducible strain components with respect to the new axes (XYZ) are given in Table II. These new irreducible strains are complex quantities and are related to the strains in the coordinate system defining the octahedral basis by the same unitary transformation that relates the d-electron basis functions in these two coordinate systems.[2,3] We emphasize that the strain components in both Tables I and II refer to an unperturbed octahedral basis; they are merely related by a coordinate transformation.

The independence of each irreducible set of symmetry-adapted strains emerges from the orthogonality of bases of IR's with respect to each other. An arbitrary strain at

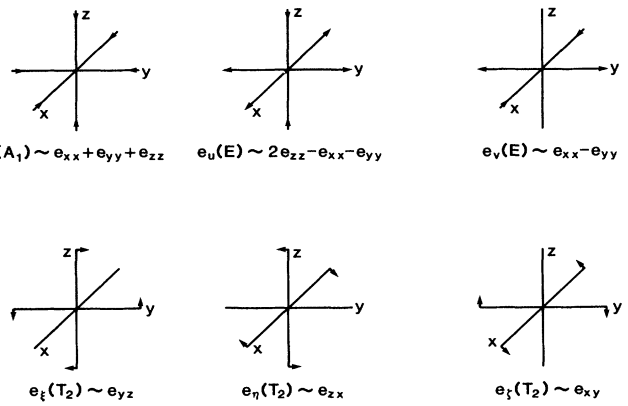

FIG. 2. Geometric representation of the different distortions represented in Table I.

the local level around Cr^{3+} can, therefore, be split and written in terms of irreducible strains using Tables I and II.

The strain around Cr^{3+} changes the interaction Hamiltonian for the $3d^3$ electrons at Cr^{3+}, and Eq. (11) becomes

$$H_{\text{total}}=H_{\text{octahedral}}+H_{\text{trig}}+H_{\text{SO}}+H_{\text{strain}}\ , \tag{16}$$

$$H_{\text{strain}}=H_{A_1}+H_E+H_{T_2}\ , \tag{17}$$

where the three terms, on the right side of Eq. (17), represent mutually independent changes in the interaction Hamiltonian due to deformation.

By writing H_{strain} in the form shown in Eq. (17), the symmetry-related equivalent interactions can be identified. This approach, in conjunction with the Wigner-Eckart theorem [Eq. (13)] minimizes the number of parameters needed for analytic calculations. Essentially, there is one reduced matrix element for each type of irreducible strain, and these can be treated as phenomenological parameters to be obtained from the experiments. Therefore, the theory cast in the form of irreducible strains introduces three parameters. Because the ambient trigonal field can be written[2,45] as $V_{x_0}(T_{2g})$, the $V_{x_0}(T_2)$ component of H_{strain} due to the imposed deformation adds onto this ambient interaction algebraically. In subsequent calculations the last three terms in Eq. (16) are treated as perturbations with respect to $H_{\text{octahedral}}$ and the ambient trigonal field effects are appropriately subtracted out in the analysis. The model parameters are obtained solely from shock-wave, uniaxial-strain, compression data. Because the procedure we have used is independent of any microscopic model of interaction potential (e.g., point-ion model), it is expected to be successful in a wide variety of situations.

B. Strain effects on ^2E states

We now apply the procedure indicated above to understand the shock response of ruby and to derive specific relations needed for evaluating the coefficients in Sec. V. We have assumed[48] that the spin-orbit interaction does not change significantly under deformations considered here. Furthermore, this approximation appears reasonable for comparable strains under hydrostatic loading as shown by the analysis of lifetime variations[49] of R lines.

TABLE II. Irreducible strains with respect to the trigonal axes.

(1) $e(A_1)=e_{XX}+e_{YY}+e_{ZZ}$

(2) $e_{u_+}(E)=-e_{u_-}(E)=-\frac{1}{\sqrt{6}}[e_{XX}-e_{YY}-2ie_{XY}+2\sqrt{2}(e_{ZX}+ie_{ZY})]$

(3) $e_{x_+}(T_2)=-e^*_{x_-}(T_2)=\frac{1}{\sqrt{3}}\left[\frac{1}{2}(e_{XX}-e_{YY}-2ie_{XY})-\frac{1}{\sqrt{2}}(e_{ZX}+ie_{ZY})\right]$

(4) $e_{x_0}(T_2)=\frac{1}{2\sqrt{3}}(2e_{ZZ}-e_{XX}-e_{YY})$

1. *Uniaxial strain along the c axis*

A uniaxial strain along the c axis has the simple feature that the symmetry of the unit cell is not altered. So, physically, we expect this strain to essentially change the parameters characterizing the ambient spectrum. This is indeed the case.

The uniaxial strain e along the c axis in terms of the trigonal axes indicated in Fig. 1 is e_{zz}, with all other components vanishing. Using Table II, this gives the following irreducible strains:

$$e(A_1)=e\ , \tag{18a}$$

$$e_{x_0}(T_2)=\frac{e}{\sqrt{3}}\ . \tag{18b}$$

$e(A_1)$, characterizing uniform compression or tension, alters only the Racah parameters B and C. But $e_{x_0}(T_2)$ brings about changes in the ambient trigonal field and, hence, changes in v and v'. Within the t_2^3 configuration, the energy matrix due to the trigonal field and spin-orbit interaction can be written as Eq. (12) and can be calculated, similar to ambient conditions, using the Wigner-Eckart theorem in Eq. (13). The results are analytically the same as Eqs. (14) and (15), and are written in the form of a matrix as follows:

	M'	u_+		u_-	
M	M_s \ M_s'	$\frac{1}{2}$	$-\frac{1}{2}$	$\frac{1}{2}$	$-\frac{1}{2}$
u_+	$\frac{1}{2}$	$-\frac{2}{3}v^2+\frac{2}{3}v\zeta$	0	0	0
	$-\frac{1}{2}$	0	$-\frac{2}{3}v^2-\frac{2}{3}v\zeta$	0	0
u_-	$\frac{1}{2}$	0	0	$-\frac{2}{3}v^2-\frac{2}{3}v\zeta$	0
	$-\frac{1}{2}$	0	0	0	$-\frac{2}{3}v^2+\frac{2}{3}v\zeta$

(19)

All of the matrix elements have a common denominator $[\epsilon(^2T_2)-\epsilon(^2E)]$ and the parameter v is given as

$$v=v_0+\Delta v\ . \tag{20}$$

Δv represents the strain-induced change in the trigonal field, and v_0 is the ambient trigonal field. Recall that $v=-3K$ to get Eqs. (14) and (15). Appropriate terms from the above matrix should be added to the function representing energy of ^2E states in terms of the Racah parameter, to account for the changes caused by $e(A_1)$.

For uniaxial strain along the c axis, $e(A_1)$ only contributes to a shift of the R lines, while $e_{x_0}(T_2)$ contributes to both the shift and the change in R_1-R_2 splitting.

2. *Uniaxial strain along the a axis*

Uniaxial strain e along the a axis, when transformed to the trigonal coordinate system (XYZ) in Fig. 1, can be written as the following strain matrix:

$$\begin{bmatrix} \frac{e}{4} & \frac{-\sqrt{3}e}{4} & 0 \\ \frac{-\sqrt{3}e}{4} & \frac{3e}{4} & 0 \\ 0 & 0 & 0 \end{bmatrix}\ . \tag{21}$$

Using Table II, the symmetry-adapted strains can be constructed as

$$e(A_1)=e\ , \tag{22a}$$

$$e_{x_0}(T_2)=-\tfrac{1}{2}\frac{e}{\sqrt{3}}\ , \tag{22b}$$

$$e_{x_+}(T_2)=-e^*_{x_-}(T_2)=\frac{(1-i\sqrt{3})}{4}\frac{e}{\sqrt{3}}\ , \tag{22c}$$

$$e_{u_+}(E)=-e^*_{u_-}(E)=\frac{(1-i\sqrt{3})}{2\sqrt{2}}\frac{e}{\sqrt{3}}\ . \tag{22d}$$

When we compare Eq. (22) with Eq. (18), for the same value of applied strain e, the following results are apparent: $e(A_1)$ is the same for the two cases; $e_{x_0}(T_2)$ for

the a axis, responsible for changes in v, is half the magnitude, but of opposite sign to that for the c axis; rhombic strains $e_{x_\pm}(T_2)$ are also nonvanishing for the a-axis case. In addition, we now have strains characterized by symmetry E.

As in the case of the c axis, the uniform strain $e(A_1)$ causes only a shift of ^2E without affecting the R_1-R_2 splitting. The trigonal potentials introduced by e_{x_0} and $e_{x_\pm}$ couple ^2E and $^2T_2$ and result in a shift of ^2E. These states are also coupled, as noted in Sec. III B, by spin-orbit interaction. Hence $e_{x_\pm}$ in conjunction with spin-orbit interaction affects the splitting, which can be calculated using Eq. (12). Further, from Eq. (13) we note that for the same value, e_{x_+}-, e_{x_-}-, and e_{x_0}-induced potentials have the same reduced matrix element.

The strains of symmetry E (a component of which refers to tetragonal distortion[23,45] in the octahedral reference system) bring about an additional splitting of R-lines. The $e(E)$-induced potential $V(E)$ does not couple ^2E to the other states in the t_2^3 configuration, and therefore there is no shift of ^2E due to $V(E)$. Instead, there exist nonvanishing, first-order off-diagonal elements of $V(E)$ in the ^2E bases which cause the splitting. We represent these matrix elements $\langle {}^2Eu_+|V(E)|^2Eu_-\rangle$ by Q, where Q is a complex number representing the effects of $e(E)$-type deformation. The form of Q is indicated next.

Again, we can calculate the eigenmatrix. $e(T_2)$ contributions are obtained using Eqs. (12) and (13), and for $e(E)$ we represent the effect as Q. Thus we get the following matrix:

	M'	u_+		u_-	
M	M_s' / M_s	$\frac{1}{2}$	$-\frac{1}{2}$	$\frac{1}{2}$	$-\frac{1}{2}$
u_+	$\frac{1}{2}$	$M+\frac{2v\zeta}{3}$	$\frac{(1-i\sqrt{3})}{3\sqrt{2}}\Delta v\zeta$	$-\frac{(1+i\sqrt{3})}{3}v\Delta v+Q$	0
	$-\frac{1}{2}$	$\frac{(1+i\sqrt{3})}{3\sqrt{2}}\Delta v\zeta$	$M-\frac{2v\zeta}{3}$	0	$-\frac{(1+i\sqrt{3})}{3}v\Delta v+Q$
u_-	$\frac{1}{2}$	$-\frac{(1-i\sqrt{3})v\Delta v}{3}+Q^*$	0	$M-\frac{2v\zeta}{3}$	$-\frac{(1-i\sqrt{3})}{3\sqrt{2}}\Delta v\zeta$
	$-\frac{1}{2}$	0	$-\frac{(1-i\sqrt{3})v\Delta v}{3}+Q^*$	$-\frac{(1+i\sqrt{3})\Delta v\zeta}{3\sqrt{2}}$	$M+\frac{2v\zeta}{3}$

(23)

where

$$M\equiv-\left[\frac{2}{3}\left[v_0+\frac{\Delta v}{2}\right]^2+\frac{\Delta v^2}{3}\right]. \tag{24}$$

In this matrix all the terms involving v and/or Δv have a common denominator $[\epsilon(^2T_2)-\epsilon(^2E)]$. In all of the terms that contain Q or Q^*, a term $-\frac{3}{72}(1+i\sqrt{3})^2\Delta v^2$ is dropped, as this will be quite small compared to the other terms. The form of Q is given by

$$Q\equiv\langle {}^2Eu_+|V_{u_+}(E)+V_{u_-}(E)|^2Eu_-\rangle$$
$$=-\frac{(1+i\sqrt{3})}{4}\frac{1}{\sqrt{3}}\langle {}^2E\|V_E(e)\|^2E\rangle . \tag{25}$$

The last factor in this equation is a reduced matrix element for the strain e and is denoted as Q_1. Hence

$$\frac{Q}{e_{u_-}}=\frac{Q^*}{-e_{u_+}}=\frac{1}{\sqrt{2}}\frac{Q_1}{e} . \tag{26}$$

Equations (25) and (26) show that Q, in general, is a complex number. As before, terms from the above matrix have to be added to the function representing ^2E states in terms of the Racah parameter, to account for the changes caused by $e(A_1)$.

Despite the complicated nature of the matrix for the a axis, the off-diagonal elements do not remove the full degeneracy. This is because the states corresponding to R_1 and R_2 lines already have the minimal degeneracy, namely, Kramers' degeneracy.[45] To lift this degeneracy, the perturbing Hamiltonian must destroy time-reversal symmetry. However, none of the strain-induced potentials has this feature, and therefore each state is still a Kramers' doublet.

Δv entering in the matrix in (23) is the same as in (20) for the same strain e. Therefore, one can diagonalize the matrix in (23), and from the splitting data along the a axis, Q can be obtained. In Sec. V we shall use the ideas developed in this section to explain the experimental results in ruby.

V. ANALYSIS OF EXPERIMENTAL RESULTS

In this section all of the experimental results pertaining to the response of ruby R lines to external stresses and strains are analyzed in a consistent manner. The parameters needed for the theoretical analysis are obtained only from the uniaxial-strain-compression data along the c and a axes. The same are then used to analyze the remainder of the shock data, hydrostatic stress, and uniaxial-stress results.

A. Evaluation of parameters

As discussed in Sec. IV, there are essentially three parameters—one for each type of symmetry-adapted representation of strain. The shift associated with $e(A_1)$-type strain is characterized by one parameter. $e(E)$-type strain introduces splitting, but no shift, and is characterized by Q. $e(T_2)$-type strain brings about changes in splitting and contributes to the shift. In principle, the splitting and shift changes for $e(T_2)$ are related to each other by relations like (14) and (15) (for the c axis). To keep the theoretical framework general and independent of experimental accuracy or relations like (14) and (15), we shall introduce two parameters to characterize $e(T_2)$-type strain. The first characterizes the shift associated with the trigonal field change per unit trigonal strain. The second characterizes the change in R_1-R_2 splitting per unit trigonal strain. These two parameters are determined from the uniaxial-strain-compression data along the c axis. The evaluation of the parameter Q shall be postponed until we discuss the R_1-R_2 splitting for uniaxial-strain compression along the a axis.

To evaluate the parameter characterizing the shift associated with uniform strain $e(A_1)$, we proceed as follows. For uniform strain e, the strain tensor can be expressed as

$$\begin{bmatrix} e/3 & 0 & 0 \\ 0 & e/3 & 0 \\ 0 & 0 & e/3 \end{bmatrix} .$$

This strain tensor can be expressed as a sum of strain tensors representing strain $e/3$ along the c axis, $e/3$ along the a axis, and $e/3$ along the m axis. It can be shown[50] that the response for the same strain magnitude along the m and a axes is the same. Hence the shift of the average of R_1 and R_2 lines due to $e(A_1)$ can be expressed as

$$e(A_1)_{\text{shift}} = \tfrac{1}{3}(\text{shift for strain along } c \text{ axis} + 2\times \text{shift for strain along } a \text{ axis}) . \quad (27a)$$

This result may be seen directly from Eqs. (18) and (22): If the strain along the a axis is doubled and added to the strain along the c axis, the trigonal strain, source of the additional shift, vanishes. As indicated,[50] e_{x_+} and e_{x_-} do not contribute. Applying Eq. (27a) to the measured average shift of the R_1 and R_2 lines for compressive uniaxial strain along the c and a axes [see Eqs. (3) and (5) in Sec. II] in the linear approximation, we obtain the parameter characterizing A_1-type of strain:

$$\Pi(A_1) = -1977.5\pm 32 \text{ cm}^{-1}/\text{density compression} . \quad (27b)$$

The negative sign indicates a redshift.

By combining the above result with the linear term in Eq. (3), we can see that the decreasing trigonal field, due to uniaxial-strain compression along the c axis, results in a blueshift of 372.8 ± 38 cm^{-1} per unit density strain. Using Eq. (18b), this corresponds to a blueshift of

$$\Pi(e_{x_0}) = 645.7\pm 66 \text{ cm}^{-1}/\text{trigonal strain} . \quad (27c)$$

From the experimental results for splitting in Eq. (4), we can write down the change in R_1-R_2 splitting from the ambient splitting value in terms of trigonal strain as

$$\Delta(R_2\text{-}R_1) = -384e_{x_0} + 530.5e_{x_0}^2 . \quad (28)$$

e_{x_0} is the trigonal strain given by Eq. (18b), and we have ignored the second-order term in Eq. (28) in subsequent calculations. For strain magnitudes considered in the present work, this approximation is reasonable. Equations (27c) and (28) show that a positive trigonal strain, as per the convention defined at the beginning of Sec. IV, results in a blueshift of the mean of R_1 and R_2 lines and a decrease in line splitting with respect to the ambient value; a positive trigonal strain causes a decrease in the trigonal field.

Using the parameters derived above and substituting them in the eigenmatrix in Eq. (23), the measured R_1-R_2 splitting for uniaxial compression strain along the a axis can be analyzed to determine Q. From Eqs. (22) and (25), we note that Q is a complex number and depends on the applied strain e in a complicated manner. In view of this, we discuss the evaluation of Q after the discussion of R_1-R_2 splitting for shock compression along the a axis.

B. Shock propagation along the c axis

1. Compression

The average shift and splitting results were used to obtain the parameters as discussed above. The one new result in the shock-compression data is that the average of the shift of the two R lines varies nonlinearly with mean stress in contrast to the hydrostatic data. Here we show that the variation of R_1-R_2 splitting observed under shock loading is consistent with the observed curvature of the average R-line shifts. Further, because the curvature for compression and tension is the same, the following analysis is also valid for the tension results. For subsequent analysis of the hydrostatic measurements, it is convenient to recast the experimental results along the c axis in terms of the mean stress $\bar{\sigma}$ ($\equiv \sigma_{mm}/3$):

$$\Delta R_1(\text{cm}^{-1}) = 0.88 - 0.6115\bar{\sigma} - 0.0025\bar{\sigma}^2 , \quad (29)$$

$$\Delta R_2(\text{cm}^{-1}) = -0.41 - 0.708\bar{\sigma} - 0.0022\bar{\sigma}^2 . \quad (30)$$

These equations also give the change in R_1-R_2 splitting as a function of mean stress. These results, along with Eq. (15), can be used to obtain the change in the trigonal

field. Taking the ambient trigonal field[6] as 800 cm^{-1} and $\epsilon(^2T_2)-\epsilon(^2E)=6734$ cm^{-1},[25] we can obtain the variation of v ($=-3K$) with mean stress as

$$v=800-2.607\bar{\sigma}+8.3\times10^{-3}\bar{\sigma}^2 . \quad (31)$$

Substituting Eq. (31) in Eq. (14) [or equivalent in terms of v in Eq. (19)], we can calculate the shift due to the changes in trigonal field, and this gives a calculated coefficient of the $\bar{\sigma}^2$ term in the shift expression as 2×10^{-3}. This compares well with the observed average curvature for R_1,R_2 lines, which is 2.35×10^{-3}.

The above calculation suggests that the curvature of the mean of the R_1,R_2 line shifts result from a variation in the trigonal field and is consistent with the splitting changes. Despite the good numerical agreement shown here, we emphasize only the qualitative agreement. This is because the observed results of R_1-R_2 splitting have considerable scatter around the fitted curve.

2. Tension

From Eq. (18) we see that both uniform and trigonal strain change sign in tension. Hence a blueshift of 1977.7 cm^{-1}/ density compression is obtained for uniform strain $e(A_1)$ in tension. The trigonal field increases in tension (e_{x_0} is negative) with the consequent increase in splitting given by Eq. (28). The c-axis results in Sec. II show that, to within the linear term, the tension and compression results for the average shift and splitting are of equal magnitude, but opposite in sign. Hence the present analysis explains quantitatively all of the tension results including the curvature.

Finally, we can examine the source of the asymmetric behavior of the mean shift for uniaxial tensile strain along the c axis with respect to uniform tension (extrapolation of hydrostatic data to tension). This asymmetry arises due to the variation in the trigonal field. The shift due to uniform compression can be identified with the hydrostat (to a good approximation) and can be written as

$$\Delta\nu_{\text{uniform}}=-\alpha\mu , \quad (32)$$

where μ is the density compression defined in Sec. II and α is a parameter that fits the data. Using Eqs. (14) and (28), the shift due to trigonal field variation can be written as

$$\Delta\nu_{\text{trig}}=\beta\mu-\gamma\mu^2 . \quad (33)$$

The total shift for uniaxial strain along the c axis is given by sum of Eqs. (32) and (33). Because β and γ are positive numbers, the two terms in Eq. (33) have opposing contributions under compression, and the mean of R_1- and R_2-line shifts under shock loading are close to the hydrostatic compression data. In tension both terms in Eq. (33) are negative and, therefore, reduce the blueshift due to uniform tension. Consequently, the shock results in tension deviate away from the extrapolated hydrostatic response curve and give rise to the asymmetry.

C. Shock propagation along the a axis

Because the experimental results from shock-wave propagation along the a axis[19] exhibit more complexity, this subsection is organized somewhat differently than Sec. V B. From Sec. II we see that for shock propagation along the a axis, the mean of the R_1- and R_2-line shifts in tension are close to the extrapolation of the hydrostatic data. Thus the asymmetry arises for a-axis propagation in compression in contrast to the c-axis data.

1. Compression: curvature and asymmetry

All of the diagonal elements in the eigenmatrix in Eq. (23) have a common term, denoted by M, which represents a shift of the mean of the R_1 and R_2 lines due to rhombic strains of the T_2 symmetry. This term is given by

$$M=-\frac{\frac{2}{3}(v_0+\Delta v/2)^2+\Delta v^2/3}{\epsilon(^2T_2)-\epsilon(^2E)} . \quad (34)$$

For a given strain e, the Δv entering in Eq. (34) is the same as the Δv for uniaxial strain e along the c axis. Assuming a second-order variation with mean stress as in Eq. (31), we have

$$\Delta v=\alpha_1\bar{\sigma}+\alpha_2\bar{\sigma}^2 . \quad (35)$$

The numerator of Eq. (34) can then be written as

$$\tfrac{1}{3}\{2[v_0+\tfrac{1}{2}(\alpha_1\bar{\sigma}+\alpha_2\bar{\sigma}^2)]+(\alpha_1\bar{\sigma}+\alpha_2\bar{\sigma}^2)^2\} .$$

Thus the terms proportional to $\bar{\sigma}^2$ are

$$\frac{2}{3}\left[\frac{\alpha_1^2\bar{\sigma}^2}{4}+v_0\alpha_2\bar{\sigma}^2\right]+\frac{1}{3}\alpha_1^2\bar{\sigma}^2=\frac{1}{2}\alpha_1^2\bar{\sigma}^2+\frac{2}{3}v_0\alpha_2\bar{\sigma}^2 . \quad (36)$$

For shock along the c axis, the corresponding term is $-\frac{2}{3}(\alpha_1\bar{\sigma}^2+2v_0\alpha_2\bar{\sigma}^2)$. Hence the curvature ratio for the a and c axes is given by

$$\frac{0.75\alpha_1^2+v_0\alpha_2}{\alpha_1^2+2v_0\alpha_2} . \quad (37)$$

Taking $\alpha_2/\alpha_1=3.184\times10^{-3}$ from Eq. (31), we find that the calculated curvature for the average of the shift of the R lines, for a given mean stress, is smaller by a factor of 1.71 compared to that along the c axis. Using the calculated c-axis value of 2×10^{-3}, we have, for the a axis,

$$\text{calculated curvature}=1.17\times10^{-3} ,$$

$$\text{measured curvature}=1.04\times10^{-3} .$$

As in Sec. V B, we want to downplay the quantitative agreement and emphasize the qualitative agreement between the calculated and experimental results. The curvature is a consequence of the trigonal field changes.

The asymmetry between the mean of the R_1- and R_2-line shifts under shock loading and the hydrostatic results can be understood as follows. Comparison of Eqs. (22b) and (18b) shows that compressive strains along the a and

c axes lead to trigonal strains with different signs in the two cases. For compression along the a axis, the trigonal strain from Eq. (22b) is negative or tensile; for tension along the a axis, the trigonal strain is positive. Because of this feature, the two terms in Eq. (33) have the same sign in compression, but tend to cancel in tension. Thus, in contrast to the c-axis results, we predict that the mean of the R-line shifts will deviate away from the hydrostat in compression and be closer to its extrapolation in tension. This is indeed the case as discussed in Sec. II. This change in asymmetry between the hydrostatic results and the shock results for the two orientations demonstrates that it is caused by changes in the trigonal field.

2. R_1-R_2 splitting in compression: evaluation of Q

As mentioned in Sec. II, the observed changes in R-line splitting for shock compression along the a axis[19] are considerably larger than for shock compression along the c axis.[17] This larger splitting arises due to additional rhombic distortions Eq. (22c) and E-type of strains [Eq. (22d)]. In general, the eigenmatrix in Eq. (23) needs to be diagonalized to evaluate the R-line splitting. However, the form of the matrix in Eq. (23) along with the assumption that changes in splitting are small compared to ambient splitting (valid for small strains) permits some simplification. Using the procedure indicated in the Appendix, the square of the R_1-R_2 splitting can be expressed as

$$\Delta^2=\frac{(\frac{4}{3}v\zeta)^2}{A^2}+\frac{8(\Delta v\zeta)^2}{9A^2}+4\left|\frac{-(1+i\sqrt{3})v\Delta v}{3A}+Q\right|^2, \tag{38a}$$

where $A=\epsilon(^2T_2)-\epsilon(^2E)\simeq 6734\ \text{cm}^{-1}$, $v=v_0+\Delta v$, and v_0, the ambient value,[6] is the same as used earlier (800 cm^{-1}). As indicated above and in Eq. (22b), trigonal strain is negative or tensile for compression along the a axis. Hence Δv is positive (leading to a larger trigonal field, $v>v_0$) and is half the value due to the same magnitude of tensile strain along the c axis; compare Eqs. (18b) and (22b). Thus all the terms on the right side of Eq. (38a), except for Q, are known from the c-axis data. Using the experimentally measured value of splitting for a-axis compression,[19] Eq. (38a) can be solved for Q:

$$\frac{Q_1}{e}=3638.7\ \text{cm}^{-1}\quad\text{or}\quad\frac{Q}{e_{u\_}}=-2572.93\ \text{cm}^{-1}. \tag{38b}$$

Evaluation of Q along with Eqs. (27b), (27c), and (28) provides all the parameters needed to evaluate wavelength changes in the R lines for an imposed deformation.

3. Analysis of tension results

The average of the R_1- and R_2-line shifts for uniaxial-strain tension along the a axis[19] is given by Eq. (5). The applied strain is decomposed into a uniform tension (A_1 strain) and a trigonal strain. By adding the blueshift due to uniform tension and the blueshift due to the trigonal term [see Eqs. (27b) and (27c)], the calculated blueshift in tension matches the linear term in Eq. (5) very well. The curvature of the average of R_1- and R_2-line shifts is the same as in compression and, as discussed in Sec. V C 1, is in good agreement with the calculated data. The analysis of the R-line splitting is discussed next.

4. R_1-R_2 splitting in tension and compression

Unlike shock propagation along the c axis, the R_1-R_2 splitting increases both in compression and tension for shock propagation along the a axis. The splitting, at small strains, is larger for compression than tension;[19] at higher strains, both sets of data show a nonlinear increase. These results can be understood as follows.

From Eq. (38a) we note that the last term on the right side is predominately symmetric with respect to a change of sign of the strain; a small term proportional to Δv^2 can be ignored. The second term on the right side is also symmetric with respect to a change of sign of the strain. Hence the splitting change between compression and tension can be written, at small strains, as

$$\Delta^2|_{\text{comp}}-\Delta^2|_{\text{tens}}=\frac{16\zeta^2}{9A^2}(v^2_{\text{comp}}-v^2_{\text{tens}}). \tag{39}$$

Because of the relationship between the trigonal strain and trigonal field parameter v discussed earlier, $v_{\text{comp}}>v_{\text{tens}}$, and therefore the splitting in compression is larger than the splitting in tension.

The magnitude of the splitting difference in Eq. (39), because it depends only on the trigonal field, can be obtained directly from the shock compression results along the c axis. For example, at a density compression of 0.827%, the splitting for a-axis compression is 33.35 cm^{-1}; this represents an increase of $\Delta|_{\text{comp}}=3.75\ \text{cm}^{-1}$ over the ambient value. The right side of Eq. (39) can be calculated entirely from the c-axis results discussed earlier: By writing Eq. (15) in terms of v and using Eqs. (22b) and (28), the value of v_{comp} and v_{tens} can be obtained for a density compression of 0.827% along the a axis. These values when substituted in Eq. (39) along with $\Delta|_{\text{comp}}=3.75\ \text{cm}^{-1}$ result in a calculated value of $\Delta|_{\text{tens}}=2.1\ \text{cm}^{-1}$. This value is in good agreement with the measured value of 2.0 cm^{-1}. Thus, for small strains, Eq. (39) describes the splitting differences adequately.

Positive definiteness of the change in splitting is also contained in Eq. (38a). The last two terms are always positive definite, irrespective of the sign of the strain. Only the first term can decrease in magnitude in tension, but it is not the dominant term.

D. Hydrostatic compression of ruby

To analyze the static compression data, we obtain the strain states corresponding to the applied stresses. We can then use the theoretical formalism developed here to predict the hydrostatic and uniaxial-stress results, and compare these predictions with the experimental observations.

The point-group symmetry for ruby, associated with the space group $R\bar{3}c$, is $\bar{3}m$. For this point group, the strain is related to the stress using the following relation:

$$\begin{bmatrix} e_1 \\ e_2 \\ e_3 \\ e_4 \\ e_5 \\ e_6 \end{bmatrix} = \begin{bmatrix} s_{11} & s_{12} & s_{13} & s_{14} & 0 & 0 \\ s_{12} & s_{11} & s_{13} & -s_{14} & 0 & 0 \\ s_{13} & s_{13} & s_{33} & 0 & 0 & 0 \\ s_{14} & -s_{14} & 0 & s_{44} & 0 & 0 \\ 0 & 0 & 0 & 0 & s_{44} & -2s_{14} \\ 0 & 0 & 0 & 0 & -2s_{14} & 2(s_{11}-s_{12}) \end{bmatrix} \begin{bmatrix} \sigma_1 \\ \sigma_2 \\ \sigma_3 \\ \sigma_4 \\ \sigma_5 \\ \sigma_6 \end{bmatrix} , \tag{40}$$

where s_{ij} represent the compliance constants and for Al_2O_3 these have been measured by Gieske and Barsch;[51] other reported values are given in Ref. 41. All the quantities in Eq. (40) are referred to the crystallographic system, and the usual convention for expressing stresses, strains, and elastic constants in the matrix notation is used.[42]

For hydrostatic loading, $\sigma_1=\sigma_2=\sigma_3$, and all other stresses are zero in Eq. (40). For $\sigma_1=\sigma_2=\sigma_3=$unity, the strains are given by

$$e_1=e_2=s_{11}+s_{12}+s_{13} , \tag{41a}$$

$$e_3=s_{13}+s_{23}+s_{33} , \tag{41b}$$

$$e_4=e_5=e_6=0 . \tag{41c}$$

The above set of strains are in the crystallographic system. However, transformation to the trigonal system (XYZ in Fig. 1) does not change the strains because of the equality of e_1 and e_2. The same result can be seen from symmetry considerations.

From the above equations, we note that hydrostatic stress does not correspond to hydrostatic strain, as expected. By substituting the compliance constants,[51] we find that e_3 is greater than e_1 by approximately 10.6%. This result is in agreement with the observation by Kottke and Williams[40] that the c axis is approximately 11% more compressible than the a axis. For an applied hydrostatic pressure of 100 kbar, the symmetry-adapted strains can be written using Table II:

$$\text{uniform strain: } e(A_1)=2e_1+e_3 =0.3933\times10^{-1} , \tag{42a}$$

$$\text{trigonal strain: } e_{x_0}(T_2)=\frac{1}{\sqrt{3}}(e_3-e_1) =0.007\,79\times10^{-1} , \tag{42b}$$

$$e_{x_+}(T_2)=e_{x_-}(T_2)=e_{u_+}(E)=e_{u_-}(E)=0 . \tag{42c}$$

Using the parameters in Eqs. (27b), (27c), and the strain values given above, the shift of the mean of R_1 and R_2 lines is given as

predicted mean shift $=-0.773$ cm^{-1}/kbar ,

observed mean shift $=-0.76$ cm^{-1}/kbar ,

where the observed mean shift is from Ref. 10. Using Eq. (28) and the trigonal strain value in Eq. (42b), the change in R_1-R_2 splitting is given as

predicted decreases in splitting $=0.003$ cm^{-1}/kbar ,

observed decreases in splitting $=0.0025\pm0.004$ cm^{-1}/kbar ,

where the observed decrease is from Ref. 10. It is clear from these results that the theoretical predictions are in excellent agreement with the experimental measurements. The predicted change in splitting is within experimental error and is too small to be observed.

E. Uniaxial-stress compression of ruby

1. Stress along the c axis

For uniaxial stress along the c axis, $\sigma_3\neq0$, and all other components are zero. Using Eq. (40), the strain tensor for unit stress can be written as

$$[e]=\begin{bmatrix} s_{13} & 0 & 0 \\ 0 & s_{13} & 0 \\ 0 & 0 & s_{33} \end{bmatrix} . \tag{43}$$

The strains in Eq. (43) are written with respect to the crystallographic system. However, as was the case for hydrostatic loading, transformation to the trigonal system (XYZ in Fig. 1) leaves the strains unchanged. Using Table II, the symmetry-adapted strains can be written as

$$e(A_1)=2s_{13}+s_{33} , \tag{44a}$$

$$e_{x_0}(T_2)=\frac{1}{\sqrt{3}}(s_{33}-s_{13}) , \tag{44b}$$

$$e_{x_+}(T_2)=e_{x_-}(T_2)=e_{u_+}(E)=e_{u_-}(E)=0 . \tag{44c}$$

Only the uniform and trigonal strains are nonvanishing. Using the compliance constants from Ref. 51, the strain values for $\sigma_3=1$ kbar are

$$e(A_1)=0.1401\times10^{-3} , \tag{45a}$$

$$e_{x_0}(T_2)=0.1477\times10^{-3} . \tag{45b}$$

Using Eqs. (27b), (27c), (45a), and (45b), the mean redshift due to uniform compression is 0.277 cm^{-1}/kbar and the mean blueshift due to the trigonal field is 0.095 cm^{-1}/kbar. Therefore, the results are

predicted mean shift $=-0.182$ cm^{-1}/kbar ,

observed mean shift $=-0.215\pm0.01$ cm^{-1}/kbar ,

where the observed mean shift is from Ref. 15.

Although this agreement is quite good, the difference between these two numbers is larger than any other set of results. We note that the statistical precision due to the trigonal field is ± 66 cm^{-1}. Using the lowest value in the 95% confidence limits, we get a predicted mean shift of -0.191 cm^{-1}/kbar, which is closer to the observed value; the use of this lower bound does not impair the other agreements. Finally, we point out that uniaxial-stress measurements are obtained for very small stress values and, therefore, have more room for error.

The splitting for uniaxial-stress compression along the c axis can be calculated by combining Eqs. (28) and (45b) and is in excellent agreement with the experimental measurements:

predicted decrease in splitting $=0.057$ cm^{-1}/kbar ,

observed decrease in splitting

$=0.058\pm0.003$ cm^{-1}/kbar ,

where the observed decrease is from Ref. 15.

2. *Stress along the a axis*

For unit stress along the a axis ($\sigma_{11}\neq 0$) and all other stresses being zero, the strain matrix in the crystallographic system is given as

$$\begin{bmatrix} s_{11} & 0 & 0 \\ 0 & s_{12} & \frac{1}{2}s_{14} \\ 0 & \frac{1}{2}s_{14} & s_{13} \end{bmatrix} . \tag{46}$$

Unlike the strains in Eqs. (41) and (43), this strain tensor is changed upon transformation to the trigonal system (XYZ in Fig. 1); the transformation consists of a 60° rotation about the z axis. In the trigonal system, the strain tensor is given by

$$\begin{bmatrix} \frac{1}{4}(s_{11}+3s_{12}) & \frac{\sqrt{3}}{4}(-s_{11}+s_{12}) & \frac{\sqrt{3}}{4}s_{14} \\ \frac{\sqrt{3}}{4}(-s_{11}+s_{12}) & \frac{1}{4}(3s_{11}+s_{12}) & \frac{s_{14}}{4} \\ \frac{\sqrt{3}}{4}s_{14} & \frac{s_{14}}{4} & s_{13} \end{bmatrix} . \tag{47}$$

From the matrix in (47), we can again write down the symmetry-adapted strains using Table II. Numerical magnitudes are obtained using the compliance constants in Ref. 51:

$$e(A_1)=s_{11}+s_{12}+s_{13}=0.1266 , \tag{48a}$$

$$e_{x_0}(T_2)=\frac{1}{2\sqrt{3}}(2s_{13}-s_{11}-s_{12})=-0.069\,975 , \tag{48b}$$

$$e_{x_+}(T_2)=\frac{1}{4\sqrt{3}}\left[(i\sqrt{3}-1)(s_{11}-s_{12})-\frac{s_{14}}{\sqrt{2}}(\sqrt{3}+i)\right]$$
$$=(-0.0524+i0.0714)=-e_{x_-}^{*} , \tag{48c}$$

$$e_{u_+}=\frac{-1}{\sqrt{6}}\left[\frac{1}{2}(s_{11}-s_{12})(i\sqrt{3}-1)+\frac{s_{14}}{\sqrt{2}}(\sqrt{3}+i)\right]$$
$$=(0.095\,774\,6-i0.088\,482\,7)=-e_{u_-}^{*} . \tag{48d}$$

For convenience, σ_1 was taken to be 1 Mbar in writing the above values. For $\sigma_1=1$ kbar, all of the numerical values in Eqs. (48a)–(48d) should be multiplied by 10^{-3}.

From the discussion of uniaxial-strain compression along the a axis in Secs. IV B 2 and V C 1 [see Eqs. (23), (24), and (34) in particular], the contributions of e_{x_+} and e_{x_-} to the mean shift are proportional to $(\Delta v)^2$. Because this is a very small change, it can be ignored in the present case. Hence the main contribution to the shift of the mean of R_1 and R_2 lines arises from strains in Eqs. (48a) and (48b). Using these equations in conjunction with Eqs. (27b) and (27c), the mean redshift due to uniform strain is 0.2504 cm^{-1}/kbar and the mean redshift due to trigonal strain is 0.0452 cm^{-1}/kbar. Therefore, the results are

predicted mean shift $=-0.296$ cm^{-1}/kbar ,

observed mean shift $=-0.28\pm0.01$ cm^{-1}/kbar ,

where the observed mean shift is from Ref. 15.

For calculating splitting for uniaxial stress along the a axis, we need to use Eq. (38a). The first term on the right side of Eq. (38a) is due to trigonal strain. The contribution of the second term, because of $(\Delta v)^2$, is negligible. The contribution of the last term can be evaluated using the Q value in Eq. (38b). The splitting calculation gives a nonlinear increase with compression: At 1 kbar we have a splitting rate of 0.0322 cm^{-1}/kbar; at 2 kbar the splitting rate is 0.0376 cm^{-1}/kbar. Using an average value, we get

predicted increase of splitting $=0.035$ cm^{-1}/kbar ,

observed increase of splitting

$=0.038\pm0.004$ cm^{-1}/kbar ,

where the observed increase is from Ref. 15. Both the mean shift and splitting results show excellent agreement between theory and experiment.

VI. DISCUSSION AND CONCLUSIONS

The present work provides a theoretical framework for calculating R-line shifts in ruby for an imposed deformation. Because the developments are quite general, they are expected to have broader applicability. As long as the general theoretical approach described in Sec. IV is applicable, it may be used to relate spectroscopic results to mechanical deformations. Thus macroscopic deformations can be analyzed in terms of local-site-symmetry changes. We also emphasize that shock data, though convenient, are not necessary for obtaining the relevant model parameters. The principal advantage of the shock experiments is that they provide well-defined strain states along the crystal orientations of interest.

One issue not discussed so far is the configuration interaction (CI).[44] As mentioned in Sec. III B, the CI of the

^2E state with higher excited states has been ignored in writing Eqs. (14) and (15). These equations represent 85% of the total contribution due to the trigonal field.[44] In principle, the inclusion of CI is likely to change these equations somewhat. But the consequent predictions do not necessarily provide better agreement with the experimental results. Irrespective of this matter, most of our analysis, except the explanation of the curvature of the redshift, is independent of Eqs. (14) and (15). It is primarily for this reason that in Sec. V we introduced two parameters: one to explain the shift associated with trigonal field and the other to describe the splitting change with trigonal field. This procedure incorporates configuration interaction implicitly. In the region of modest strains, v and v' are expected to change linearly with strain; thus shift and splitting parameters represent two independent equations of appropriate form even in the presence of configuration interaction.

The present work has interesting implications for pressure calibration at very high pressures in diamond anvil studies. Under nonhydrostatic loading, knowledge of the relative orientation between the crystal axes and stress components is needed for an accurate analysis. To the best of our knowledge, oriented ruby chips are not used in diamond-anvil-cell measurements. We recommend that the use of oriented ruby crystals, if feasible, be explored in high-pressure measurements because such usage would permit separation of effects due to stress gradients from those due to crystal orientation and nonhydrostatic loading, and lead, therefore, to improved pressure calibration.

In the absence of oriented ruby chips, the use of the R_2 line as a pressure calibrant has been recommended[52] in DAC studies. The present analysis can be used to understand qualitatively the observed[52] insensitivity of the R_2-line shift, for a given density compression, to crystal orientation and nonhydrostatic stresses. Under purely hydrostatic loading, uniform strain [$e(A_1)$ type] totally dominates and the trigonal strain [$e(T_2)$ type] contribution is negligible (see Sec. V D). Hence both R lines shift equally, and the redshift [Eq. (27b)] arises due to changes in Racah parameters because of density compression.

Uniaxial strain, in contrast, leads to a strongly nonhydrostatic state.[17–19] As indicated in Sec. IV, the imposed strain along the c and a axes consists of $e(A_1)$ and other types of strain. The effect of $e(A_1)$ causes a redshift of the mean of R_1 and R_2 lines (^2E) as just discussed. For c-axis compression, the trigonal strain magnitude is significant and results in a blueshift of the mean [Eq. (27c)] and a decrease in splitting of the lines [Eq. (28)]. For the higher-energy R_2 line, these trigonal strain effects tend to cancel and the overall change is the redshift due to density compression as in hydrostatic loading. For a-axis compression, there exists $e(T_2)$- and $e(E)$-type strains as indicated in Eq. (22). The increase in splitting is given by Eq. (38a) and arises due to Q and an increase in v. However, the trigonal strain now has a different sign [Eq. (22b)] and leads to a redshift of the mean. Again, for the higher-energy R_2 line, the splitting increase and redshift of the mean tend to cancel each other and the overall change is the redshift due to density compression as in hydrostatic loading. For the R_1 line, the contributions add in both cases and the overall change is not just due to density compression. We emphasize that the analysis in Sec. V can be used to quantitatively evaluate the discussion presented here. At compressions much greater than those discussed here, incorporation of higher-order strains in the theory need to be considered. This is expected to be relatively straightforward because nonhydrostatic stresses beyond the range of present shock experiments are unlikely due to yielding. Hence only $e(A_1)$-type strains need to be considered at higher compressions.

The present work also opens up the possibility of understanding shock deformation at the local level. As indicated in Ref. 19, the Hugoniots of sapphire, representing a continuum response, are indistinguishable for shock loading along the a and c axes, yet the R-line data, analyzed here, show large differences. Thus the optical data are more sensitive than continuum measurements to changes at the microscopic level. The ability to analyze the data in terms of site symmetry changes underscores the use of dopant ions to study the environment around the ion to understand shock-induced changes at the atomic and/or molecular level. For shocked solids this is an exciting possibility. We are currently working on extending the optical measurements to stress ranges beyond the yield limit to understand inelastic deformation at a microscopic level.

In conclusion, a theoretical framework has been developed to relate changes in the ruby R-line data to imposed deformation for a broad range of loading conditions. Our approach is based on the general framework of crystal-field theory and avoids the assumption of an approximate description like the point-ion model. However, the use of a generalized approach requires the use of some experimental data to evaluate the relevant parameters in the model. The ability to predict results of experiments very different from those used to obtain the model parameters provides significant credibility to the theoretical developments. We close by emphasizing that the success of the theoretical developments was not expected when we started this work and has been very gratifying.

ACKNOWLEDGMENTS

We have benefited greatly from numerous discussions and interactions with other colleagues involved in the ruby work: Jim Burt, Xiao-An Shen, and Paul Horn. Without their experimental efforts, the present work could not have been carried out. This work was carried out under ONR Contract No. N00014-86-K-0307, and one of us (Y.M.G.) would like to acknowledge Dr. R. S. Miller for his encouragement and support in addressing this important but difficult problem.

APPENDIX

The matrix in Eq. (23) has the following form:

$$\begin{bmatrix} A & C & D & 0 \\ C^* & B & 0 & D \\ D^* & 0 & B & C \\ 0 & D^* & C^* & A \end{bmatrix} . \tag{A1}$$

We shall solve it using a perturbation approximation; that is, $|C|$ and $|D|$ are small compared to the diagonal terms. We also consider the perturbation terms sequentially. First, $C \neq 0$ and $D=0$, and then D is made nonzero.

For $C \neq 0$ and $D=0$, the matrix has a block diagonal form and the eigenvalues are solutions of the following quadratic equation:

$$(A-\epsilon)(B-\epsilon)-|C|^2=0 . \tag{A2}$$

Solving for ϵ, we get

$$\epsilon=\frac{(A+B)\pm[(A-B)^2+4|C|^2]^{1/2}}{2} . \tag{A3}$$

If we represent the eigenvalues as A' and B', then

$$A'-B'=[(A-B)^2+4|C|^2]^{1/2} . \tag{A4}$$

We now switch on the interaction term D, and the matrix takes the form

$$\begin{bmatrix} A' & 0 & D & 0 \\ 0 & B' & 0 & D \\ D^* & 0 & B' & 0 \\ 0 & D^* & 0 & A' \end{bmatrix} . \tag{A5}$$

The interaction D between the states A' and B' can be seen as indicated by the submatrices. We can rewrite this matrix by permuting the basis appropriately to give the following diagonal matrix:

$$\begin{bmatrix} A' & D & 0 & 0 \\ D^* & B' & 0 & 0 \\ 0 & 0 & B' & D \\ 0 & 0 & D^* & A \end{bmatrix} . \tag{A6}$$

As before, the eigenvalues of this matrix are

$$\epsilon'=\frac{(A'+B')\pm[(A'-B')^2+4|D|^2]^{1/2}}{2}$$
$$=\frac{(A+B)\pm[(A-B)^2+4(|C|^2+|D|^2)]^{1/2}}{2} . \tag{A7}$$

This result has been used in writing Eq. (38) in the text. In effect, the procedure used here assumes that in the first diagonalization ($C \neq 0, D=0$), the value of D does not change. In reality, D changes to D'. But the correction term will be proportional to CD or C^2. Hence, for our problem, the correction term to D will be proportional, to the lowest order, to the square of the strain and can be neglected.

*Present address: High Pressure Physics Section, Bhabha Atomic Research Center, Bombay, India.

[1]S. Sugano and I. Tsujikawa, J. Phys. Soc. Jpn. **13**, 899 (1958).
[2]S. Sugano and Y. Tanabe, J. Phys. Soc. Jpn. **13**, 880 (1958).
[3]D. S. McClure, J. Chem. Phys. **36**, 2757 (1962).
[4]J. Margerie, C. R. Acad. Sci. **255**, 1598 (1962).
[5]S. Sugano and M. Peter, Phys. Rev. **122**, 381 (1961).
[6]R. M. Macfarlane, J. Chem. Phys. **39**, 3118 (1963).
[7]D. E. Rimmer and D. F. Johnston, Proc. Phys. Soc. **89**, 943 (1966); **39**, 953 (1966).
[8]R. A. Forman, G. J. Piermarini, J. D. Barnett, and S. Block, Science **176**, 284 (1972).
[9]G. J. Piermarini, S. Block, J. D. Barnett, and R. A. Forman, J. Appl. Phys. **46**, 2774 (1975).
[10]R. G. Munro, G. J. Piermarini, S. Block, and W. B. Holzapfel, J. Appl. Phys. **57**, 165 (1985).
[11]H. K. Mao, P. M. Bell, J. W. Shaner, and D. J. Steinberg, J. Appl. Phys. **49**, 3276 (1978).
[12]J. A. Xu, H. K. Mao, and P. M. Bell, Science **232**, 1404 (1986).
[13]A. Jayaraman, Rev. Mod. Phys. **55**, 65 (1983).
[14]A. L. Schawlow, in *Advances in Quantum Electronics,* edited by T. R. Singer (Columbia University Press, New York, 1961), p. 50.
[15]E. Feher and M. D. Sturge, Phys. Rev. **172**, 244 (1968).
[16]P. D. Horn and Y. M. Gupta, Appl. Phys. Lett. **49**, 856 (1986).
[17]P. D. Horn and Y. M. Gupta, Phys. Rev. B **39**, 973 (1989).
[18]Y. M. Gupta, P. D. Horn, and J. A. Burt (unpublished).
[19]X. A. Shen and Y. M. Gupta (unpublished).
[20]S. Ohnishi and S. Sugano, Jpn. J. Appl. Phys. **21**, L309 (1982).
[21]X. Shangda, G. Changxin, L. Libin, and D. E. Ellis, Phys. Rev. B **35**, 7671 (1987).
[22]R. M. Macfarlane, Phys. Rev. **158**, 252 (1967).
[23]A. L. Schawlow, A. H. Pikisis, and S. Sugano, Phys. Rev. **122**, 1469 (1961).
[24]Surinder M. Sharma and Y. M. Gupta, Phys. Rev. B **40**, 3329 (1989).
[25]R. G. Munro, J. Chem. Phys. **67**, 3146 (1977).
[26]D. P. Ma, X. T. Zheng, Y. S. Xu, and Z. G. Zhang, Phys. Lett. A **115**, 245 (1986).
[27]D. P. Ma, J. R. Chen, Z. Q. Wang, and Z. G. Zhang, Phys. Lett. A **126**, 377 (1988).
[28]J. H. Eggert, K. A. Goettel, and I. F. Silvera, Phys. Rev. B **40**, 5724 (1989).
[29]D. R. Stephens and H. G. Drickamer, J. Chem. Phys. **35**, 427 (1961).
[30]E. Duval, R. Louat, and R. Lacroix, Phys. Status Solidi **50**, 627 (1972).
[31]R. Lacroix, E. Duval, B. Champagnon, and R. Louat, Phys. Status Solidi **68**, 473 (1975).
[32]B. Champagnon and E. Duval, J. Phys. C **13**, 131 (1980).
[33]R. A. Forman, B. A. Weinstein, and G. Piermarini, in *Spectroscopie des Elements de Transition et des Elements Lourds Daus Les Solids,* Proceedings of Colloques Internationaux Centre National de la Researche Scientifique, Lyon, France, 1976 (CNRS, Paris, 1977), Vol. 255, p. 51.
[34]R. W. G. Wyckoff, in *Crystal Structures,* 2nd ed. (Interscience,

New York, 1964).
[35]S. C. Moss and R. E. Newnhan, Z. Kristallogr. **120**, 359 (1964).
[36]James W. McCauley and G. V. Gibbs, Z. Kristallogr. **135**, 453 (1972).
[37]H. d'Amour, D. Schiferl, W. Denner, H. Schulz, and W. B. Holzapfel, J. Appl. Phys. **49**, 4411 (1978).
[38]L. W. Finger and R. M. Hazen, J. Appl. Phys. **49**, 5823 (1978).
[39]Y. Sato and S. I. Akimoto, J. Appl. Phys. **50**, 5285 (1979).
[40]T. Kottke and F. Williams, J. Appl. Phys. **54**, 6749 (1983).
[41]G. Simmons and H. Wang, in *Single Crystal Elastic Constants and Calculated Aggregate Properties: A Handbook* (MIT, Cambridge, MA, 1971).
[42]"Standard on piezoelectric crystals, 1949," Proc. IRE **37**, 1378 (1949).
[43]H. D. Megaw, *Crystal Structures: A Working Approach* (Saunders, Philadelphia, 1973), pp. 226–231.
[44]R. M. Macfarlane, J. Chem. Phys. **47**, 2066 (1967).
[45]S. Sugano, Y. Tanabe, and H. Kamimura, *Multiplets of Transition Metal Ions in Crystal* (Academic, New York, 1970).
[46]M. H. L. Pryce and W. A. Runciman, Discuss. Faraday Soc. **26**, 34 (1958).
[47]For example,

$$\phi_u' = -\frac{\sqrt{3}}{2}\phi_u - \frac{1}{2}\phi_v \sim y^2 - z^2 ,$$

$$\phi_v' = \frac{\sqrt{3}}{2}\phi_u - \frac{1}{2}\phi_v \sim z^2 - x^2 .$$

[48]The spin-orbit interaction parameter is $\approx 270\ \mathrm{cm}^{-1}$ for a free Cr ion [J. Owen, Proc. R. Soc. London, Sect. A **227**, 183 (1955)]. At ambient conditions it is estimated (Ref. 6) to be $170\ \mathrm{cm}^{-1}$ in ruby crystal. Therefore, it is expected that a few percent change in the density will not affect this parameter very strongly.
[49]Surinder M. Sharma and Y. M. Gupta, Appl. Phys. Lett. **54**, 84 (1989).
[50]When the eigenmatrix of the type in Eq. (23) is written for a strain e along the m axis, we find that changes due to strain along the m axis are the same as due to strain along the a axis. This is expected because $e(A_1)$ and $e_{x_0}(T_2)$ remain the same, and e_{x_+} and e_{x_-} change sign when strain is applied along the m axis instead of the a axis.
[51]J. H. Gieske and G. R. Barsch, Phys. Status Solid **29**, 121 (1967).
[52]Y. M. Gupta and X. A. Shen, Appl. Phys. Lett. (to be published).